Geochimica et Cosmochimica Acta 422 (2026) 360–371

Contents lists available at ScienceDirect

Geochimica et Cosmochimica Acta

journal homepage: www.elsevier.com/locate/gca

Extreme negative Eu anomalies in peraluminous granites of South China: implications for extensive fluid extraction☆

Zi Ye[a,*], Ming Tang[a], Xu Chu[b,c]

[a] SKLab-DeepMinE, MOEKLab-OBCE, School of Earth and Space Sciences, Peking University, China
[b] Department of Earth Sciences, University of Toronto, Toronto, ON M5S 3B1, Canada
[c] State Key Laboratory of Lithospheric and Environmental Coevolution, University of Science and Technology of China, Hefei, China

ARTICLE INFO

Co-Guest Editor: Xiao-Ming Liu

ABSTRACT

Mesozoic peraluminous granites in South China (aluminum saturation index >1.0) often exhibit strong Eu depletions. These extreme Eu anomalies (Eu/Eu* down to <0.01) are observed primarily in the early Yanshanian period, coeval to extensive W-Sn mineralization in the area (162–141 Ma), but the origin of such extremely low Eu/Eu* remains elusive. Here, we analyzed representative Mesozoic granite samples from South China for whole rock major and trace elements, zircon U-Pb ages, trace elements, and oxygen isotopes. Our results suggest that the amount of sediment incorporation is insufficient to generate the extremely low Eu/Eu*. If plagioclase retention played a major role in achieving such low Eu/Eu*, oxygen fugacities of <FMQ–5 would be required, even under conditions of extreme feldspar retention and fractionation; such reducing conditions do not align with zircon redox indicators (FMQ–2 to FMQ+1). On the other hand, modeling results show that fluid extraction can substantially decrease Eu/Eu* in granitic melts, but the efficiency strongly depends on fluid salinity. Achieving Eu/Eu* <0.01 in residual melts requires a fluid-to-melt mass ratio of >0.2 for brine systems and >0.8 for low-salinity fluids. Correlations between the Eu/Eu* and Ba/Th and Ba/Nb ratios further support this fluid-driven mechanism. We thus propose that extensive halogen-rich fluids exsolution and extraction were critical to generating extremely low Eu/Eu* in the peraluminous granites and likely contributed to W-Sn mineralization in South China. As much of South China existed as an isolated inland sea at low latitudes in the Indosinian period, intense evaporation combined with high productivity may have formed massive halogen- and organic-rich sedimentary strata. These strata were buried to deep crustal level during the Early Jurassic in response to the low-angle subduction of the Paleo-Pacific Plate. We further propose that reworking of these sedimentary strata provided halogens and other volatiles essential for the magmatism and W-Sn mineralization during the early Yanshanian period.

1. Introduction

Peraluminous granites, with aluminum saturation indices (ASI = $Al_2O_3/(CaO + Na_2O + K_2O)$ in mole) greater than 1.0, are key indicators of crustal reworking and magmatic differentiation (Lehmann, 1990; Brown and Pitfield, 2014, Lehmann, 2021; Zhang et al., 2023a). In South China, the Nanling region saw extensive emplacement of peraluminous granites during the Mesozoic, particularly in the early Yanshanian period (Zhou et al., 2006; Huang et al., 2015; Zhang et al., 2023c). Many of these early Yanshanian granites are associated with W-Sn mineralization (Yuan et al., 2019; Zhao et al., 2022a).

One intriguing feature of the peraluminous granites in the Nanling region is their extreme negative Eu anomalies (expressed as Eu/Eu*, chondrite normalized $Eu/(Sm \times Gd)^{1/2}$). Many of these granites exhibit extremely low Eu/Eu* values, down to <0.01 (Chen et al., 2018; Wu et al., 2023). Such extreme Eu/Eu* are rare in peraluminous granites from other magmatic periods in South China, such as the Indosinian granites (ca. 250–200 Ma), and are also uncommon in peraluminous granites from other regions, including those in the Himalayan orogen (Gao et al., 2017; Cao et al., 2022).

Traditional explanations for negative Eu anomalies emphasize plagioclase fractional crystallization/retention (Henderson, 1984;

☆ This article is part of a special issue entitled: 'In honor of Bill McDonough' published in Geochimica et Cosmochimica Acta.

* Corresponding author.
E-mail address: zye0702@stu.pku.edu.cn (Z. Ye).

https://doi.org/10.1016/j.gca.2025.07.028
Received 25 February 2025; Accepted 28 July 2025
Available online 31 July 2025
0016-7037/© 2025 Elsevier Ltd. All rights are reserved, including those for text and data mining, AI training, and similar technologies.

Gelman et al., 2014; Chen et al., 2023). The role of fluids during the magmatic-hydrothermal transition has also been suggested (Bau, 1996; Irber, 1999; Monecke et al., 2011; Ballouard et al., 2016). However, there is still no consensus on whether the distinctively low Eu/Eu* in evolved granites are the result of extreme fractional crystallization or fluid extraction. In particular, how the interplay of redox conditions, magmatic processes, and fluid involvement may influence Sm-Eu-Gd fractionation has not been adequately explored. The markedly low Eu/Eu* observed in granites formed in the early Yanshanian period also raises questions about the geological processes unique to that interval.

In this study, we investigate the processes responsible for the extremely low Eu/Eu* in Mesozoic peraluminous granites from South China. We analyze whole rock major and trace elements to characterize Eu/Eu* in granites and perform zircon U-Pb dating and trace element analyses to reconstruct system oxygen fugacities. We then develop quantitative models to evaluate the relative contributions of plagioclase fractionation and fluid extraction under the oxygen fugacities from zircon proxies. We also assess the contribution of sedimentary materials to the magma Eu/Eu* using zircon oxygen isotopes. Finally, we place our observations in the context of geological and geographical evolution of the South China region, offering insights into potential connections between extremely low Eu/Eu*, paleoenvironmental reconstruction, tectonic transitions, and W-Sn mineralization.

2. Geological background and samples

The South China Block (SCB) formed between 850 and 900 Ma through the amalgamation of two major blocks: the Yangtze Block in the northwest and the Cathaysia Block in the southeast, along the Jiangshan-Pingxiang and Pingxiang-Longkang faults (Fig. 1a, b) (Li et al., 2009a; Shu et al., 2015). The SCB underwent multiple geological events, including Paleozoic orogeny (Lin et al., 2018), Triassic collisions with North China and Indosinia (Meng and Zhang, 2000; Lin et al., 2005), and extensive lithospheric reworking and magmatism during the Late Mesozoic (Zhou et al., 2006; Li and Li, 2007; Liu et al., 2020b). These processes culminated in the formation of a highly evolved crust of South China.

During the Mesozoic, the lithosphere of the SCB experienced alternating periods of compression and extension, which played a key role in shaping Mesozoic Basin-and-Range-style magmatic province in South China (Wang et al., 2013; Song et al., 2016; Ji et al., 2018). However, the driving mechanisms of these processes remain debated. Two prevailing hypotheses have been proposed: (1) a convergent margin model, where flat subduction of the Paleo-Pacific plate was followed by slab foundering (Li and Li, 2007; Li et al., 2019) and rollback (Zhou and Li, 2000; Dai et al., 2020); (2) a lithospheric delamination and intra-continental extension model, in which the SCB underwent lithospheric thinning irrelevant to subduction (Wang et al., 2008; Deng et al., 2019; Zhang et al., 2023b).

Mesozoic igneous rocks are extensively distributed in the southeastern SCB, particularly across the Cathaysia Block and eastern Yangtze Block, playing a pivotal role in the region's geological evolution (Fig. 1b; Zhou et al., 2006; Hu and Zhou, 2012). The central Cathaysia Block, particularly the Nanling Range, is recognized as a focal point of Late Mesozoic magmatism, especially during the early Yanshanian period (Mao et al., 2013; Li et al., 2018; Yuan et al., 2019; Hu et al., 2024a). The Nanling region hosts numerous composite granite plutons, such as the Guposhan, Qianlishan, and Qitianling plutons, along with numerous small yet highly differentiated granitic intrusions, which are often spatially and genetically associated with significant W-Sn polymetallic deposits (Fig. 1b; Chen et al., 2021; Wu et al., 2023).

We collected 27 Mesozoic granite samples from the Nanling Range, including 2 Triassic (Indosinian) granites and 25 Jurassic-Cretaceous (Yanshanian) granites, with sampling sites located within intrusions

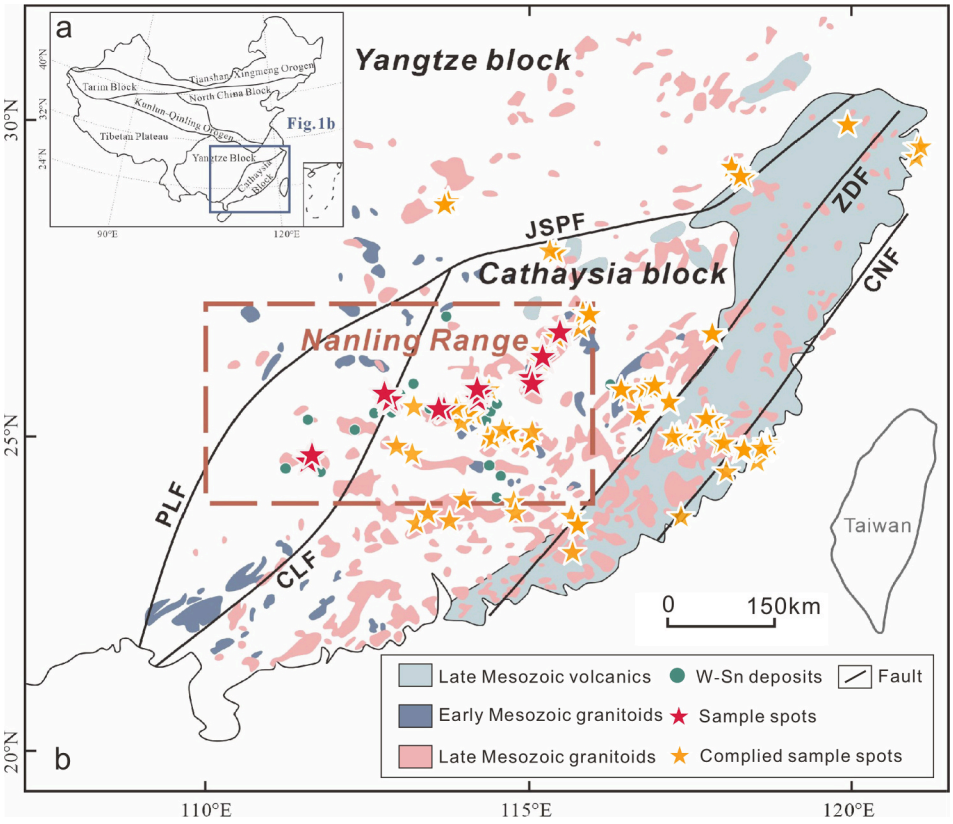


Fig. 1. (a) Major tectonic units of China. (b) Simplified geological map of South China illustrating the spatial distribution of Mesozoic igneous rocks and sample locations (modified after Hu et al., 2024b). Faults: JSPF, Jiangshan-Shaoxing-Pingxiang fault; PLF, Pingxiang-Longkang fault; CLF, Chenzhou-Linwu fault; ZDF, Zhenghe-Dapu fault; CNF, Changle-Nan'ao fault.

such as the Qitianling, Guposhan, Jiufeng plutons, and others (Fig. 2). The distribution of sampling locations is illustrated in Fig. 1b, and the detailed coordinates of the sampling points are listed in (Table S1 in Supplementary Material 1). For comparison, we also included four leucogranites from Himalaya orogen. The granite samples are relatively fresh, and the weathered and alteration portions were carefully removed. A small number of the samples contain phenocrysts (Fig. 2). The mineral assemblages typically consist of quartz (~45–55 vol%), plagioclase (~20–30 vol%), K-feldspar (~15–25 vol%), biotite (~5–10 vol%), and minor muscovite (<5 vol%). Accessory minerals include zircon, apatite, and trace amounts of iron oxides. The granites exhibit typical equilibrium granitic textures, with anhedral to subhedral plagioclase and interstitial quartz, and perthitic textures commonly observed in K-feldspar (Fig. S1 in Supplementary Material 3). Biotite occurs as subhedral flakes intergrown with feldspars. In addition, Numerous fluid inclusions are present within quartz, some containing daughter minerals that are possibly halite, although further analysis is needed to confirm this speculation (Fig. S1c in Supplementary Material 3).

3. Methods

3.1. Major and trace element analyses

All samples selected for whole rock analyses were fresh without apparent alteration or mineralization. Whole rock analyses were conducted at Wuhan SampleSolution Analytical Technology Co., Ltd. Bulk major element analyses were performed using a Rigaku ZSX Primus II wavelength-dispersive X-ray fluorescence spectrometer (XRF) equipped with a 4.0 kW end-window rhodium target X-ray tube. The operating conditions were set to 50 kV for voltage and 60 mA for current. The Kα lines were used for all major elements. Calibration curves were established using certified reference materials, including the GBW07101-14 rock series, GSS07401-08 soil series, and GBW07302-12 stream sediment series. Data correction was conducted using the theoretical α-coefficient method, and the relative standard deviation (RSD) of the analyses was less than 2 %. The trace element concentrations of bulk rock samples were determined using an Agilent 7700e ICP-MS. Whole rock ferrous oxide analysis was conducted using the potassium dichromate volumetric method at Wuhan SampleSolution Analytical Technology Co., Ltd., Wuhan, China. The analysis adhered to the standards outlined in the chemical analysis methods for silicate rocks (Part 14). Samples were decomposed using hydrofluoric and sulfuric acids, and boric acid was added to the complex residual fluorine. Sodium

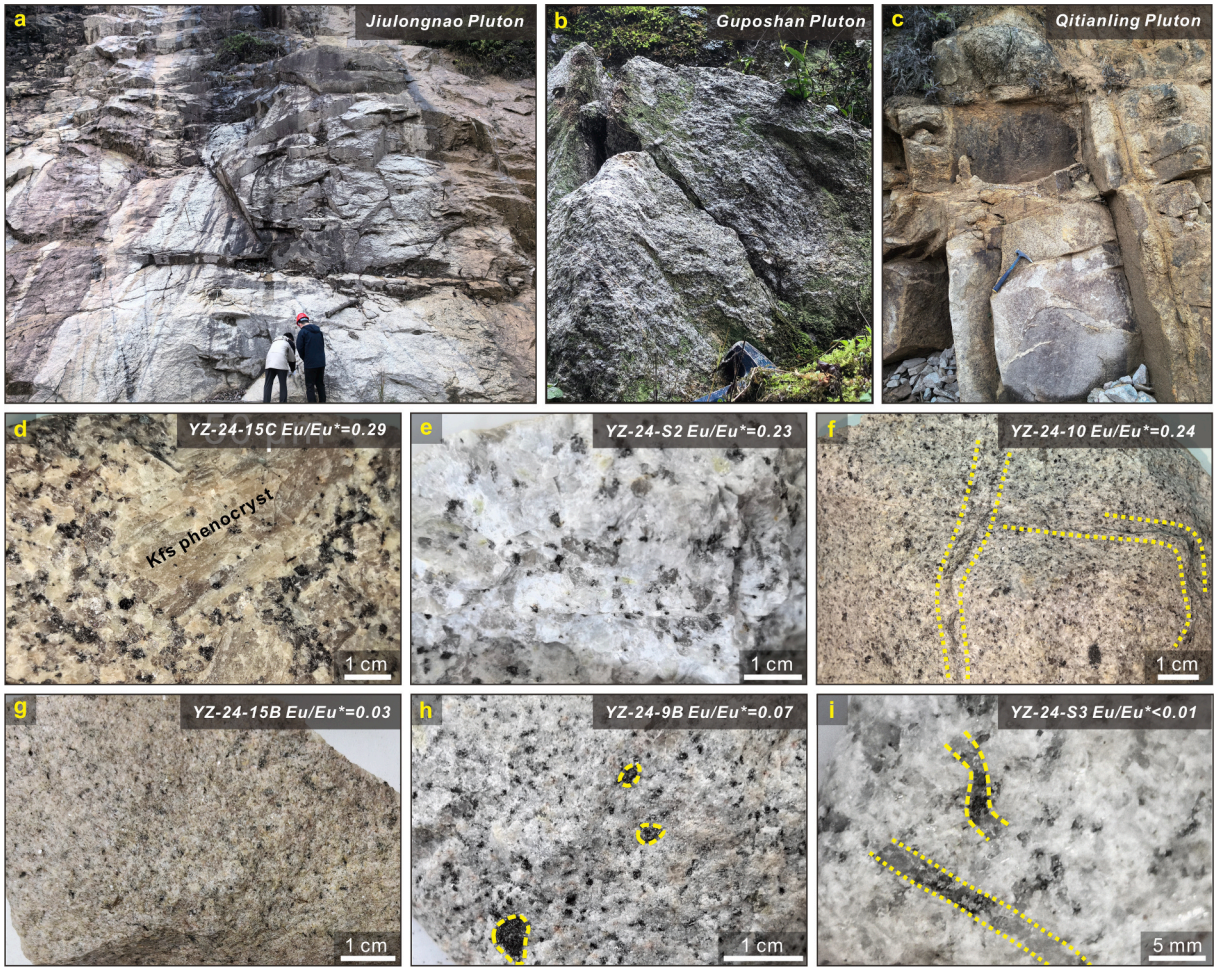


Fig. 2. Photographs of granite outcrops and samples. (a) Field outcrop of the Jiulongnao pluton, developing veins. (b) Field outcrop of the Guposhan pluton. (c) Field outcrop of the Qitianling pluton, with fresh rocks showing minimal weathering. (d) Biotite granite with K-feldspar phenocrysts (YZ-24-15C), exhibiting moderately low Eu/Eu*. (e) Fine-grained two-mica granite (YZ-24-S2), showing moderately low Eu/Eu*. (f) Biotite granite (YZ-24-10) with dark-colored veins exhibiting moderately low Eu/Eu*. (g) Biotite granite (YZ-24-15B) showing low Eu/Eu*. (h) Granite (YZ-24-9B) containing black enclaves exhibiting low Eu/Eu*. (i) Two-mica granite (YZ-24-S3) with extremely low Eu/Eu* (down to <0.01), containing fine veins. Chemical analyses were performed on vein-free areas.

diphenylamine sulfonate served as the indicator, and potassium dichromate was used as the titrant. The ferrous oxide content was subsequently calculated based on the titration results.

We also compiled a dataset of whole rock major and trace element analyses for over 2500 granitic samples, including the Indosinian and Yanshanian granites from South China and leucogranites from Himalaya. Peraluminous granites were identified using the Aluminum Saturation Index (ASI > 1), and highly evolved granites were further filtered based on SiO_2 content exceeding 70 wt%. A total of 1870 data meeting these criteria were selected for subsequent analysis and comparison.

3.2. SIMS oxygen isotope analyses

Zircon grains were separated from the rock samples, mounted, and polished at Beijing Zhongke MineResearch Testing Technology Co., Ltd. Cathodoluminescence (CL) imaging was carried out using a MIRA3 field-emission scanning electron microscope (FE-SEM) operated at an accelerating voltage of 7 kV and a 2-minute scanning time, producing high-resolution CL images with clear zoning patterns. Based on transmitted and reflected light microscopy and CL images, measurement points were selected on zircon grains at locations that were free of surface cracks, had well-defined internal zoning, and lacked inclusions.

Oxygen isotope measurements were performed using a CAMECA IMS 1300-HR3 secondary ion mass spectrometer (SIMS) at the State Key Laboratory for Mineral Deposits Research, Nanjing University, China. The analysis used a $^{133}Cs^+$ primary ion beam with a total impact energy of 20 keV and was conducted in Gaussian mode. To minimize the ablation depth, a 5 μm raster mode was employed during the analysis, while charge compensation was achieved using a normal-incidence electron gun. Magnetic field stabilization was ensured using NMR field sensors. The ion transfer system was set to a magnification of × 75 to enhance ion transmission efficiency. The mass resolving power (MRP, M/ΔM), defined at 50 % peak width, was adjusted to ~2500 to mitigate isobaric interference. The signals for ^{16}O and ^{18}O were simultaneously recorded by two Faraday cups at positions L'2 (1010 Ω) and H'2 (1011 Ω), respectively. The typical signal intensities were approximately 2×10^9 cps for $^{16}O^-$ and 4.5×10^6 cps for $^{18}O^-$, with an internal precision of ~0.2 ‰ (2SE) for single oxygen isotope ($^{18}O/^{16}O$) analysis. To validate the accuracy of the SIMS methodology, oxygen isotope analyses of the Penglai and Qinghu zircon reference materials were conducted intermittently throughout the measurement period for the $\delta^{18}O$ values of the samples.

3.3. Zircon U-Pb dating and trace element analyses

After oxygen isotope analyses, zircon grains were simultaneously analyzed for their U-Pb isotopes and trace elements at Beijing Zhongkekuangyan Test Technology Co. Ltd. Zircon U-Pb isotope dating and trace element measurements were performed using LA-ICP-MS. The laser ablation system used was a RESOlution S-155 193 nm excimer laser coupled with a Thermo Fisher Element XR ICP-MS. During laser ablation, helium was used as the carrier gas, while argon served as a compensatory gas to optimize sensitivity. The gases were mixed through a Y-shaped connector before entering the ICP.

All analyses were conducted in spot mode, with a 30 μm diameter beam size, ~5 J/cm^2 energy, and 6 Hz repetition rate. Each time-resolved analytical dataset comprised approximately 15–20 s of background signal, followed by 45 s of sample signal. Dwell times were set to 20 ms for ^{207}Pb, ^{206}Pb, and ^{208}Pb, 100 ms for ^{49}Ti, ^{140}Ce, ^{147}Sm, ^{153}Eu, ^{157}Gd, and 10 ms for ^{232}Th, ^{238}U, ^{204}Pb, and other trace elements. Off-line data processing, including the selection of background and sample signals, instrument sensitivity drift correction, elemental concentration calculation, U-Th-Pb isotope ratio determination, and age calculation, was carried out using the Iolite software package (version 4.0, Paton et al., 2011).

Zircon 91,500 (1062 Ma) was used as the external standard for correcting instrumental mass discrimination and elemental fractionation during ablation. Zircon SA01 was measured as an unknown sample to assess instrument performance. GJ-1 (600 Ma) was treated as a quality control for geochronology. Trace element concentrations were calibrated using NIST610 glass as the external reference material, with silicon (Si) employed as the internal standard. 91500, NIST610, GJ-1, and SA01 were measured twice before and after 10 sample analyses. Repeated analyses of SA01 yielded mean Eu/Eu* values of 1.10 ± 0.09 (2 SD), which were consistent with recommended values of 1.15 ± 0.12 (2 SD) (Huang et al., 2019).

4. Results

4.1. Eu anomalies in peraluminous granites (measured and compiled data)

We collected and analyzed major and trace element compositions for 31 granite samples, including 25 Yanshanian granites, 2 Indosinian granites from South China, and 4 Himalayan leucogranites from southern Tibet (Table S2 in Supplementary Material 1). Granite samples with age constraints are shown as pink to red dots in Fig. 3. These data reveal that the Yanshanian granites are characterized by exceptionally low Eu/Eu* ratios, reaching below 0.01 and an averaging 0.18, in stark contrast to the Indosinian granites (0.36) and the Himalayan leucogranites (0.82). To place these findings in a broader context, we compiled published data of U-Pb ages and major and trace element compositions for Mesozoic granites in South China and leucogranites in the Himalayas (Supplementary Material 2). The South China Mesozoic granites are typically characterized by peraluminous compositions (ASI >1) and high SiO_2 contents (>70 wt%), which are representative of granites in this region. To ensure meaningful comparisons across different regions and geological periods, we applied the same filtering criteria (ASI > 1 and SiO_2 >70 wt%) to all datasets. These thresholds were selected to include only highly evolved, peraluminous granites, minimizing compositional variability and the influence of crystal fractionation on Eu/Eu*. The compiled data exhibit trends that closely match our analytical results, with extremely low Eu/Eu* (<0.01) predominantly occurring in early Yanshanian samples (especially 162–141 Ma, dark pink band in Fig. 3c). The strong agreement between our measured data (pink to red dots in Fig. 3b, c) and the compiled data (blue dots in Fig. 3b, c) indicates the extremely low Eu/Eu* values are a widespread geochemical feature of early Yanshanian magmatism and confirms that our sampled granites are representative of the regional geochemical trend.

4.2. Zircon U-Pb dating and trace element analysis

A total of 15 granite samples were analyzed (13 Yanshanian granites, 1 Indosinian granite, and 1 Himalayan granite), with approximately 20–30 zircon grains selected from each sample for U-Pb dating and trace element analysis. Most analytical spots were on zircon rims, with a few targeting zircon cores. For granites from South China, most zircon U-Pb ages range from 165 to 153 Ma, corresponding to the early Yanshanian period. This age range aligns with the magmatic and metallogenic peaks in South China and the regional tectonic extension period. Additionally, a granite sample from South China yielded a U-Pb zircon age of 230.60 Ma, within the Indosinian period. Among these samples, one leucogranite from the Himalayas yielded a zircon U-Pb age of 15.38 Ma. The data mentioned above are provided in Table S3 of Supplementary Material 1.

For trace element analyses, zircons with age concordance below 90 % were excluded. Grains with La concentrations exceeding 1 ppm, likely inherited from inclusions, were filtered out (Zou et al., 2019; Tang et al., 2020). Metamorphic zircons are excluded using a Th/U ratio cutoff of <0.1 (Hoskin and Schaltegger, 2003). The Eu/Eu* of zircons range from 0.03 to 0.38 in South China granites, showing no obvious correlation

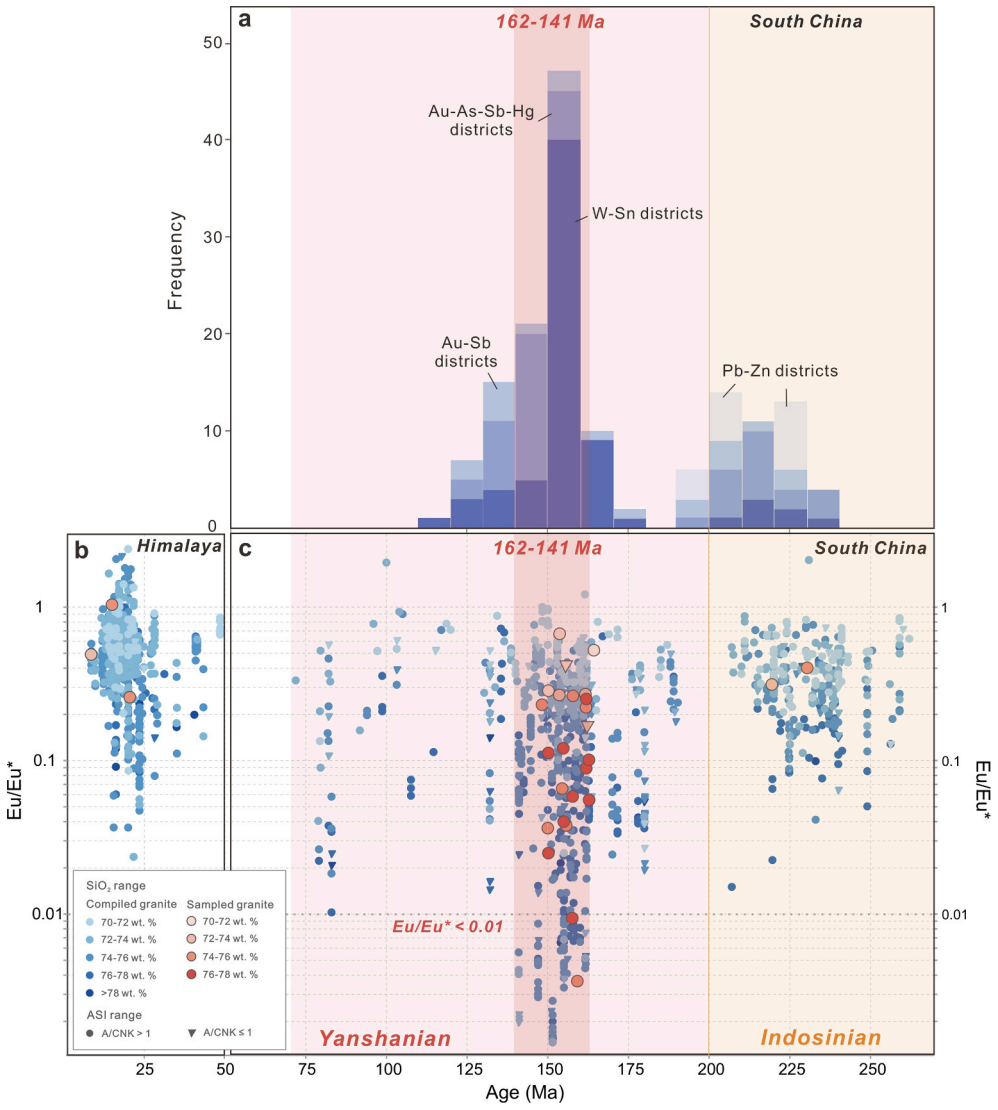


Fig. 3. (a) Age distribution histogram of Mesozoic ore deposits in South China (modified after Mao et al., 2013; Hu et al., 2024c). The frequency indicates the number of deposits within each metallogenic cluster area and the column patterns represent different types of mineralization as originally classified in that reference. Plot of Eu/Eu* versus age for granites from Himalaya (b) and South China (c). A total of 1617 data points were plotted, of which 1394 granites were classified as peraluminous granites. The orange shading represents the Eu/Eu* values of Indosinian granites in South China, while the pink shading indicates the Eu/Eu* values of Yanshanian granites in South China. The darker pink band highlights the time interval (162–141 Ma) in South China during which extremely low Eu/Eu* values (as low as <0.01) occur.

with whole rock Eu/Eu* (Table S3 in Supplementary Material 1).

After applying these filtering criteria, only 235 zircon trace element datasets were retained out of the initial 500 analyses. The filtered trace element data for zircons from each granite sample were used to calculate magmatic oxygen fugacity using the Ce-U-Ti oxybarometer (Table S3 in Supplementary Material 1) (Loucks et al., 2020). The trace element compositions of the zircon cores and rims are similar, and the calculated oxygen fugacity ranges are relatively comparable. The calculated average oxygen fugacity for the early Yanshanian granites is FMQ–0.3. Granites with whole rock Eu/Eu* >0.1 exhibit a wider range of zircon oxygen fugacity values (FMQ–2.1 to FMQ+1.3), with no clear correlation with Eu/Eu* (Fig. 4a).

4.3. Zircon oxygen isotopic compositions

The $\delta^{18}O$ values of zircons from 20 granite samples were analyzed, and the results are summarized in Table S4 of Supplementary Material 1. Among these samples, two are Himalayan leucogranites, two are Indosinian granites, and the rest are Yanshanian granites. We analyzed 10–15 zircon spots for each sample, with most analyses on the grain rims and a few on cores or mantles. Many zircons from these highly evolved granites are enriched in Th and U, which may lead to significant metamictization that complicated the interpretation of oxygen isotope data (Wang et al., 2014). Therefore, we evaluated metamictization effects on our zircon oxygen isotope measurements. Comparisons show that $\delta^{18}O$ values differ by less than 0.3 ‰ between metamictized and non-metamictized zircons (Fig. S2 in Supplementary Material 3), with no correlation observed between $\delta^{18}O$ and Th or U concentrations (Fig. S3 in Supplementary Material 3). Together with the intra-sample consistency (generally <1 ‰), these results confirm that metamictization has negligible impact on our oxygen isotope data.

Oxygen isotope analyses of zircon cores and mantles reveal a range of $\delta^{18}O$ values (6.38–12.30 ‰ VSMOW). The results indicate that for granites with Eu/Eu* <0.1, the $\delta^{18}O$ values of zircon are relatively constant, with an average of 9.0 ‰. By contrast, granites with Eu/Eu* >0.1 exhibit a wider range of zircon $\delta^{18}O$ values (8.93–11.28 ‰) that are generally higher than those observed in low Eu/Eu* granites (Fig. 4b, Table S4 in Supplementary Material 1). The average oxygen

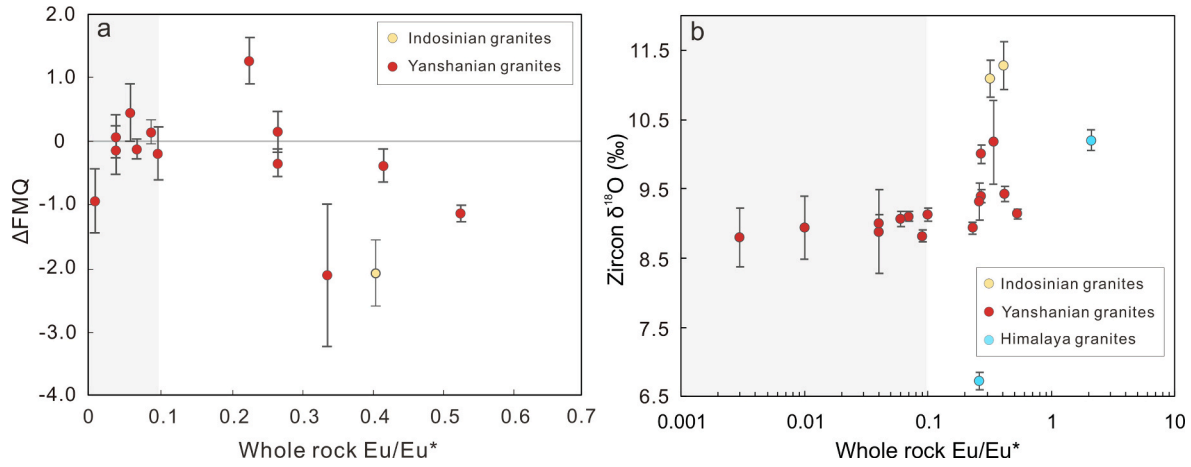


Fig. 4. (a) Plot of zircon Ce-U-Ti oxybarometer calculation results (Loucks et al., 2020) versus whole rock Eu/Eu*. Oxygen fugacity data are plotted as averages and 2 SE errors. (b) Plot of zircon oxygen isotopes versus whole rock Eu/Eu*. Oxygen isotope data are plotted as averages and 2 SE errors.

isotope values of zircons in the two Himalaya granites are 6.72 ‰ and 10.20 ‰, respectively. Additionally, there is no obvious correlation between zircon $\delta^{18}O$ values and whole rock SiO_2 content.

5. Discussion

5.1. Formation of extreme negative Eu anomalies in South China granites

Europium is a redox-sensitive element that exists in magmatic systems in two oxidation states, Eu^{2+} and Eu^{3+} (Weill and Drake, 1973). Eu^{2+} exhibits isomorphous substitution with Ca^{2+} in plagioclase and replaces K^+ in K-feldspar. Consequently, the proportion of feldspar involved in partial melting and fractional crystallization may lead to Eu depletion or low Eu/Eu* in the residual melt. The degree of Eu depletion caused by feldspar fractionation strongly depends on the redox state, which determines the relative proportions of Eu^{2+} and Eu^{3+} in the melt (Burnham et al., 2015). Another key consideration is whether the source region itself exhibits a low Eu/Eu*. Additionally, the role of fluid exsolution may also be important, as fluid extraction can selectively remove Eu^{2+} from the residual melts, further lowering Eu/Eu* (Bau, 1996; Irber, 1999; Monecke et al., 2011; Ballouard et al., 2016). In the following sections, we evaluate the relative contributions of these processes through quantitative modeling of their effects on Eu/Eu*.

5.1.1. The influence of sources

A pronounced Eu depletion in the melt may be inherited from mature clastic sediments in the source region or during assimilation, as mature clastic sediments are likely to exhibit a more significant Eu depletion than the average upper continental crust composition (Gao and Wedepohl, 1995; Rudnick and Gao, 2014; Yu et al., 2023). This possibility can be tested by oxygen isotopes. The subsequent discussion focuses on oxygen isotope data obtained from zircon rims, which are more likely to record the isotopic composition of the crystallizing magma. In contrast, cores and mantle domains may represent inherited components and are therefore excluded to avoid incorporating unrelated or pre-magmatic signatures. Zircon oxygen isotopes remain nearly constant during magmatic evolution but are sensitive to the addition of crust-derived material (Valley et al., 2005; Kemp et al., 2007; Sundell et al., 2024). Our samples with whole-rock Eu/Eu* >0.1 exhibit more variable zircon $\delta^{18}O$ values (8.93–11.28 ‰), whereas those with whole-rock Eu/Eu* <0.1 show relatively uniform but still elevated zircon $\delta^{18}O$ values (~9 ‰) (Fig. 4b). These consistently high oxygen isotope values suggest significant sedimentary contributions to the magma source. However, the lack of a negative correlation between zircon $\delta^{18}O$ and whole-rock Eu/Eu* indicates that sediment incorporation alone is not the primary control on the Eu/Eu* of these granites.

5.1.2. The influence of feldspar fractionation

Feldspar fractionation can impart low Eu/Eu* in the melt, but the extent this Eu depletion strongly depends on oxygen fugacity (Weill and Drake, 1973). The more reduced the system is, the lower melt Eu/Eu* feldspar fractionation can generate. Here, we calculate the oxygen fugacities needed to generate the extremely low Eu/Eu* in our samples by feldspar fractionation.

The calculation requires knowledge about the extent of fractional crystallization (X) and the partition coefficients of Eu in feldspar (D_{Eu}). The Eu^{2+} partition coefficients in feldspars were approximated by those of Sr (~5 in plagioclase and K-feldspar in felsic systems; Stix and Gorton, 1990; Ewart and Griffin, 1994; White, 2003; Luo et al., 2024). The partitioning of Eu^{2+} in other mineral phases was ignored if their Sr partition coefficients are much smaller than 1. The partition coefficient for Eu^{3+} was approximated using the average of neighboring REE partition coefficients (Sm and Gd), yielding $D_{Eu(III)} = D_{Sm} = D_{Gd} = 0.05$ (Fedele et al., 2015; Rollinson and Pease, 2021). It is noteworthy that previously reported partition coefficients span wide ranges and vary with analytical method, sample composition, and experimental conditions. We adopted the partition coefficients most suitable for felsic and peraluminous magmatic systems.

We used the average value of the Eu anomalies in the early Yanshanian granites with $SiO_2 \leq 70$ wt% ($Eu/Eu^*_{initial} = 0.6$, Supplementary Material 2) as that of the parental granitic magma before extensive feldspar fractionation. The extent of fractionation crystallization (X) was set to 90 % to represent an extreme differentiation scenario. This unrealistic assumption allows us to evaluate the maximum possible effect of plagioclase fractionation on Eu/Eu* and to test whether such a process alone could account for the observed extremely low Eu/Eu* within the oxygen fugacity range constrained by our zircon oxybarometer results. Fractional crystallization was performed in 90 steps with a step size of 1 %, and each step adopted a batch crystallization model under the same oxygen fugacity. The feldspar proportions during each crystallization step were taken from rhyolite-MELTS outputs under fractionate solids mode (Gualda et al., 2012). Since the Yanshanian magmatic activity is characterized by H_2O-rich (Li et al., 2009b; Chen et al., 2021; Jiang et al., 2022a), accompanied by the crystallization of hydrous minerals such as biotite and the development of numerous magmatic-hydrothermal veins, we adopted an upper limit of feldspar fractional crystallization (mass fraction = 40 %, Fig. S4 in Supplementary Material 3) under conditions where H_2O exceeds 4 wt% (Li et al., 2009b; Chen et al., 2021). The parameters used in the calculation are selected to be the most favorable for forming low Eu/Eu*, allowing for

determination of the highest oxygen fugacity required to produce extremely low Eu/Eu*. The calculation equations are listed in Supplementary Material 4.

Our modeling results show that an oxygen fugacity below FMQ is necessary to lower melt Eu/Eu* to 0.1. However, Achieving Eu/Eu* <0.01 requires an unrealistically low oxygen fugacity <FMQ–5 (Green lines in Fig. 5). Previous studies estimate that the oxygen fugacities of Yanshanian granites in South China range from FMQ–1.8 to FMQ+1.6 (Zhang et al., 2017; Guo et al., 2018; Ma et al., 2024), and zircon oxygen fugacity calculations in this study yielded comparable oxygen fugacities of FMQ–2.1 to FMQ+1.3 (Fig. 4a). In addition, metamorphism of organic carbon-bearing protoliths may buffer the oxygen fugacity at CCO of ~FMQ–1.3 at 750 ℃ (Chu and Ague, 2013), consistent with the range recorded in the zircons. These values are significantly higher than the oxygen fugacity thresholds (< FMQ–5) required for fractional crystallization to achieve Eu/Eu* <0.01. Therefore, the strongly reducing conditions (<FMQ–5) appear unlikely, which suggests that fractional crystallization alone cannot account for the observed extremely low Eu/Eu* in South China granites.

5.1.3. The influence of fluid extraction

Our calculations above show that feldspar fractionation (retention in the source and crystallization during differentiation) can hardly lower Eu/Eu* down to 0.01 seen in the South China granites. We now investigate the influence of fluid exsolution and extraction on melt Eu/Eu* since Eu^{2+} is more soluble than Eu^{3+} in magmatic fluids (Bai and Koster van Groos, 1999; Zajacz et al., 2008).

In this study, the term “fluid exsolution” refers to the process during the late stages of magmatic evolution when the silicate melt becomes saturated with volatiles (e.g., H_2O, Cl-bearing species), leading to the separation of an aqueous fluid phase from the melt. The extraction of such fluid causes efficient removal of highly soluble elements from the melt into the exsolved fluid phase. It is important to note that the fluid exsolution and extraction discussed here occur entirely above the solidus, within the magmatic system, and do not involve subsolidus hydrothermal fluid-rock interactions or alteration. This interpretation is supported by the fact that the granites analyzed are fresh and have LOI (loss on ignition) values mostly below 1 wt%, indicating negligible post-magmatic hydrothermal overprint. Therefore, the observed extremely low Eu/Eu* values are interpreted to result from magmatic fluid extraction rather than later fluid-rock alteration.

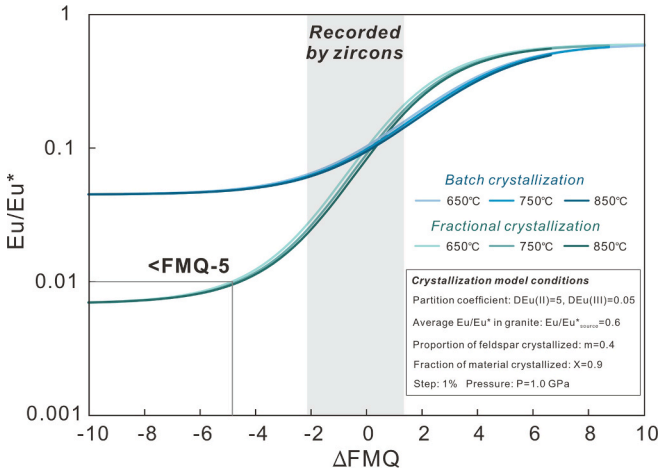


Fig. 5. The influence of oxygen fugacity on Eu/Eu* in the melt during batch and fractional crystallization. The gray shading denotes the range of oxygen fugacity calculated using the zircon oxybarometer in granite samples. The parameters used in the calculations were selected to favor the formation of low Eu/Eu*, constraining the upper oxygen fugacity limit required for generating extremely low Eu/Eu*. Under the fractional crystallization model, Eu/Eu* values in the melt can decrease to <0.01 at conditions below FMQ–5, whereas under the batch crystallization model, even at FMQ–10, Eu/Eu* values in the melt do not fall below 0.01.

In this calculation, critical parameters include the initial Eu/Eu* of the melt before fluid exsolution, the partition coefficients of Eu^{2+} and Eu^{3+} between the fluid and melt, the ratio of Eu^{2+}/Eu^{3+} ratio in the system, and the fluid-to-melt mass ratio. Since fluid exsolution occurs in late stages of magmatic evolution, we set the pre-exsolution Eu/Eu* of the melt to 0.3 that is easily achievable through feldspar fractionation (Fig. 5). The partition coefficient of Eu^{2+} was approximated using the Sr partition coefficient between fluid and felsic melt. Given the limited research on the partition coefficients of middle rare earth elements between high-salinity fluids and melts, the partition coefficient of Eu^{3+} was approximated by that of La (Drake and Weill, 1975; Zajacz et al., 2008). The partitioning of REEs between fluid and felsic melt are strongly influenced by halogen concentrations (e.g., Cl, F) in the fluid (Bai and Koster van Groos, 1999; Zajacz et al., 2008; Borchert et al., 2010). Consequently, both low-salinity (vapor or supercritical) and high-salinity (brine) fluid scenarios were considered (Fig. 6). For low-salinity fluids in peraluminous magmatic systems, $D_{Eu(II)} = D_{Sr} = 5$ and $D_{Eu(III)} = D_{La} = 0.1$, while for high-salinity fluids, $D_{Eu(II)} = D_{Sr} = 50$ and $D_{Eu(III)} = D_{La} = 0.5$ (Zajacz et al., 2008). The ratio of Eu^{2+} to Eu^{3+} in the melt is primarily controlled by the system oxygen fugacity, with the relationship established by Burnham et al. (2015). By applying mass balance and partitioning principles, the evolution of Eu/Eu* in both melt and fluid under varying oxygen fugacity (ΔFMQ) and fluid-to-melt mass ratios (M) can be modelled. The equations are listed in Supplementary Material 4.

Fluid exsolution preferentially sequesters Eu^{2+} to Eu^{3+} and thus depletes Eu in both fluid and melt with increasing fluid-melt ratio (Fig. 6). The continuous fluid extraction model allows low-salinity fluids at FMQ–0.3 (mean Yanshanian granite oxygen fugacity) to achieve a melt Eu/Eu* <0.01 for a fluid-to-melt mass ratio exceeding 0.8 (Fig. 6a). Under the same conditions, for high-salinity fluids, a fluid-to-melt mass ratio of as low as 0.2 is sufficient to generate these extreme Eu/Eu* (Fig. 6b). Thus, high-salinity fluids are more efficient in extracting Eu^{2+} from the melt (Fig. 6). This interpretation is supported by fluid inclusion studies in South China granites, which reveal a wide range of homogenization temperatures and salinities (1.4–41 wt% NaCl equiv), indicating the intense high-salinity fluid exsolution (Lu et al., 2003; Liu et al., 2020a; Bai et al., 2022). Such fluid extraction processes are likely to occur near the upper regions of magma chambers where fluid flux is higher (Shinohara et al., 1995; Luo et al., 2008). It is worth noting that fluids extracted from melts during the very early stages of magmatic evolution may exhibit a high Eu/Eu*, but this high Eu/Eu* quickly disappears with progressive fluid extraction (Fig. 6).

These modeling results demonstrate that the extraction of high-salinity fluids provides a viable mechanism for generating the extremely low Eu/Eu* values observed in early Yanshanian granites. To further explore the geochemical effects of fluid exsolution, we examine the behavior of elements with contrasting fluid mobility—such as fluid-mobile barium (Ba) and fluid-immobile thorium (Th) and niobium (Nb). Barium and Th exhibit similar compatibility in melts, while Nb is slightly more compatible than Ba (Ptáček et al., 2020). Because all three elements behave as incompatible to mildly compatible during magmatic differentiation, Ba/Th and Ba/Nb ratios generally remain stable or increase slightly during fractional crystallization, indicating that crystallization alone cannot explain the observed decreases in these ratios. However, their fluid-melt partitioning behaviors differ significantly. Eu^{2+} and Ba have comparable high-salinity fluid-melt partition coefficients of >40 and strongly partition into the fluid phase during exsolution, whereas Th and Nb have extremely low fluid-melt partition coefficients (<0.1) and remain in the melt (Zajacz et al., 2008). The strong positive correlations between Eu/Eu* and Ba/Th (Fig. 7a) and between Eu/Eu* and Ba/Nb (Fig. 7b) are consistent with Eu^{2+} and Ba being lost to the exsolved fluids, resulting in their synchronous depletions in the melt. These geochemical signatures provide strong

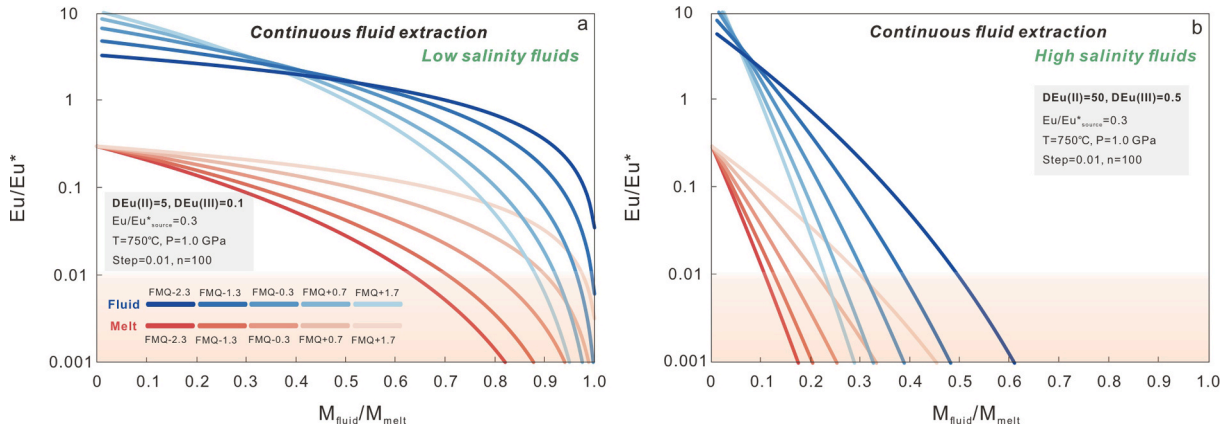


Fig. 6. Eu anomalies in the felsic melt and coexisting fluid generated through continuous exsolution and extraction of (a) low-salinity fluid and (b) high-salinity fluid. The red and blue lines represent the variations in Eu/Eu* in the melt and fluid, respectively.

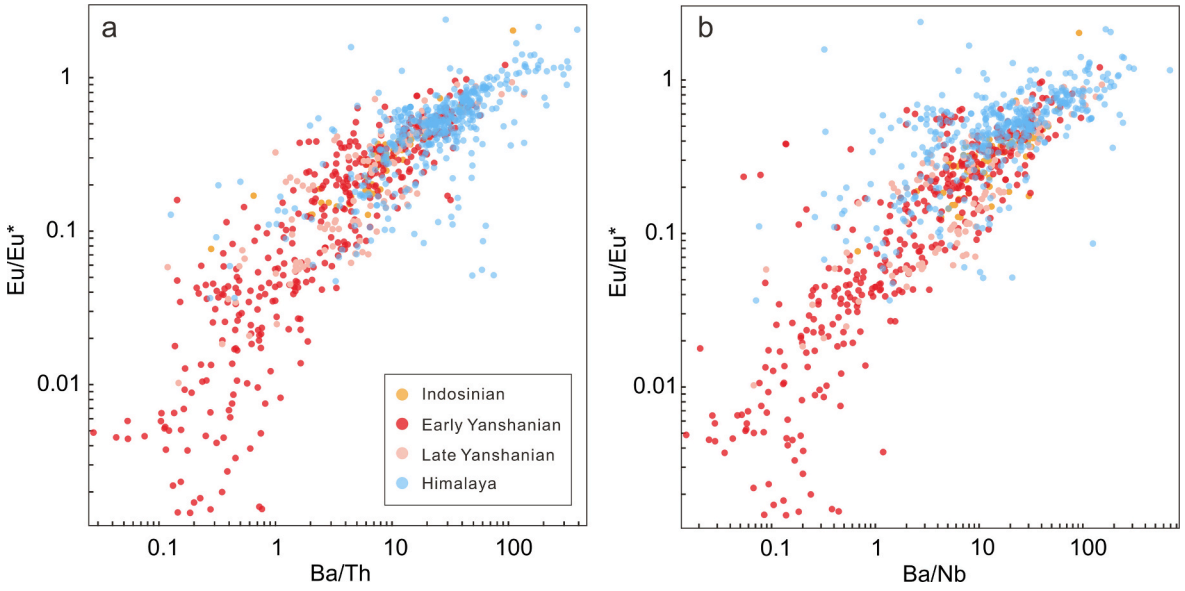


Fig. 7. Correlations between whole rock Eu/Eu* and fluid extraction indicators including (a) Ba/Th and (b) Ba/Nb.

evidence for extensive fluid extraction under mildly reducing conditions during the early Yanshanian period in South China.

5.2. *Implications for W-Sn mineralization and paleoenvironment in South China in the Mesozoic*

The close association between early Yanshanian granites (162–141 Ma) in South China and significant W-Sn mineralization (Mao et al., 2013; Xu et al., 2023; Hu et al., 2024a), along with their development of extremely low Eu/Eu* (down to <0.01) (Fig. 3), provides a unique opportunity to investigate the petrogenetic and metallogenic processes operating during this tectonic period. Since our findings point to the critical role of high-salinity fluid extraction in generating extremely low Eu/Eu* in the syn-ore forming granites, it will be interesting to examine how such extensive fluid extraction may have contributed to W-Sn enrichment and mineralization.

Tungsten and Sn in the melt form complexes with these halogens, facilitating their migration into the fluid phase and subsequent enrichment to form ore deposits (Zhao et al., 2022b). Experimental studies have shown that W, Sn, and Eu^{2+} exhibit comparable partition coefficients between peraluminous melts and high-salinity fluids (Zajacz et al., 2008), suggesting that W and Sn, like Eu^{2+}, are efficiently transferred into exsolved fluids. As a proof of concept, we calculate the partitioning of W and Sn between fluids and melt (Fig. 8, calculation equations and details are provided in Supplementary Material 4). The modeling results further indicate that during continuous fluid exsolution, W and Sn concentrations in high-salinity fluids can reach more than 40 times their initial melt contents, particularly at the early stages of extraction (Fig. 8a, b). Moreover, when Eu/Eu* in the melt decreases below 0.01, the total amounts (tonnages) of W and Sn extracted by the fluid reach a maximum and no longer increase (Fig. 8c, d), implying that progressive Eu^{2+} depletion is accompanied by substantial enrichment of W and Sn in the fluid phase. This coupled behavior indicates that high-salinity fluid exsolution not only plays a critical role in generating extreme negative Eu anomalies but also facilitates the concentration and transport of W and Sn, creating favorable conditions for their mineralization. These findings highlight that extremely low Eu/Eu* in peraluminous granites can serve as potential geochemical indicators for W-Sn exploration in South China and analogous metallogenic provinces globally.

One remaining question is what tectonic environment may have provided the halogen-rich and mildly reduced sources, critical to the formation of extremely low Eu/Eu* and possibly W-Sn mineralization in South China. South China experienced a prolonged shallow marine

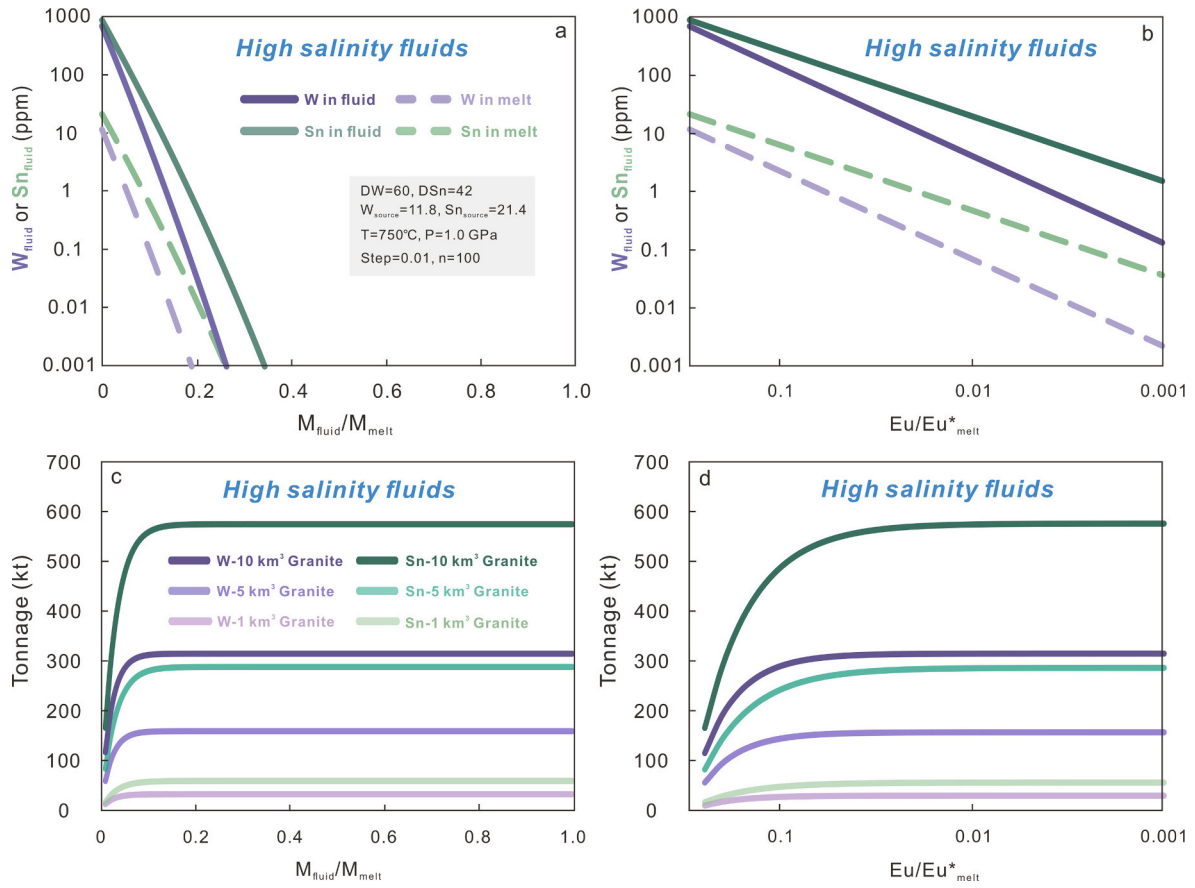


Fig. 8. (a, b) Modeled evolution of W and Sn concentrations in exsolved high-salinity fluids (solid lines) and residual melt (dashed lines) during continuous fluid extraction. Figure (a) illustrates how fluid W and Sn concentrations vary with the fluid-to-melt mass ratio, while figure (b) shows their relationship with Eu/Eu* values in the residual melt. (c, d) Calculated variations in the total amount (tonnage) of W and Sn extracted by high-salinity fluids during continuous fluid extraction from melts of different volumes. Purple-toned lines represent variations in W concentrations, while green-toned lines represent variations in Sn concentrations. For each element (W and Sn), the color gradient from dark to light indicates a decrease in the residual melt volume after fluid exsolution, from large to small (10 km^3, 5 km^3, and 1 km^3, respectively). Figure (c) shows how the total extracted mass varies with the fluid-to-melt ratio, and figure (d) presents the relationship between extracted metal tonnage and Eu/Eu* values in the residual melt.

environment from the Middle Devonian to the Middle Triassic (Xu et al., 2009; Xu, 2023), depositing extensive sequences rich in evaporites and organic carbon (Shu et al., 2008; Liu et al., 2023). Paleogeographic reconstructions using GPlates (Scotese, 2021) indicate that the region was near the equator during the Permian-Triassic (Fig. 9a), with high evaporation rates and biological productivity promoting high-salinity conditions, deposition of high-salinity sediments, organic carbon (Kasten and Jørgensen, 2000; Henson et al., 2012), and pre-enrichment of Sn and W in the protoliths (Romer and Kroner, 2016; Zhao et al., 2021). Such an equatorial setting during the Permian-Triassic was unique compared to the subsequent Jurassic-Cretaceous (Yanshanian) period, when the region had drifted northward (Fig. 9c, e) (Wang et al., 2023). During the Indosinian orogeny, South China collided with the North China and Indochina blocks (Dong et al., 2011; Faure et al., 2016; Zhao et al., 2023), followed by the progressive dominance of Paleo-Pacific plate subduction in East Asia (Li and Li, 2007; Hu and Zhou, 2012; Jiang et al., 2022b). This tectonic uplift around the margins created a relatively enclosed basin in the South China interior, forming an intracontinental saline sea, herein referred to as the Paleo South China Sea (Fig. 9b).

After the formation of high-salinity marine sediments, subsequent Indosinian orogeny and Paleo-Pacific plate subduction resulted in crustal thickening and burial of these sediments to deeper crustal levels (Fig. 9b, d) (Li and Li, 2007; Jiang et al., 2022b). We propose that reworking of the buried high-salinity strata, facilitated by Paleo-Pacific plate rollback and mantle upwelling (Fig. 9f), contributed additional volatiles to the granitic magmas, increasing their H_2O and Cl contents and thereby promoting the exsolution and extraction of high-salinity fluids during late-stage magmatic evolution. This is consistent with fluid inclusion studies reporting high-salinity fluids in South China granites (Lu et al., 2003; Liu et al., 2020a; Bai et al., 2022) and with our observation of fluid inclusions containing daughter minerals in some of the samples (Fig. S1c in Supplementary Material 3).

6. Conclusions

Extremely low Eu/Eu* values (down to <0.01) are observed in Yanshanian peraluminous granites in South China. To elucidate the petrogenesis, we assessed potential mechanisms including source inheritance, feldspar fractionation, and fluid extraction. The lack of a correlation between whole-rock Eu/Eu* and zircon oxygen isotopes suggest that the extremely low Eu/Eu* in the granites were not solely inherited from sedimentary rocks. Fractional crystallization modeling indicates feldspar fractionation would not suffice either, because achieving Eu/Eu*~0.01 requires an oxygen fugacity <FMQ–5, inconsistent with zircon records (FMQ–2 to FMQ+1). Instead, our modeling demonstrates that extensive extraction of magmatic fluids, particularly those of high salinities, under mildly reducing conditions (~FMQ–0.3, mean Yanshanian granite oxygen fugacity) plays a dominant role in generating the extremely low Eu/Eu* in the Yanshannian granites. Correlations between Eu/Eu* and Ba/Th, Ba/Nb further support this conclusion.

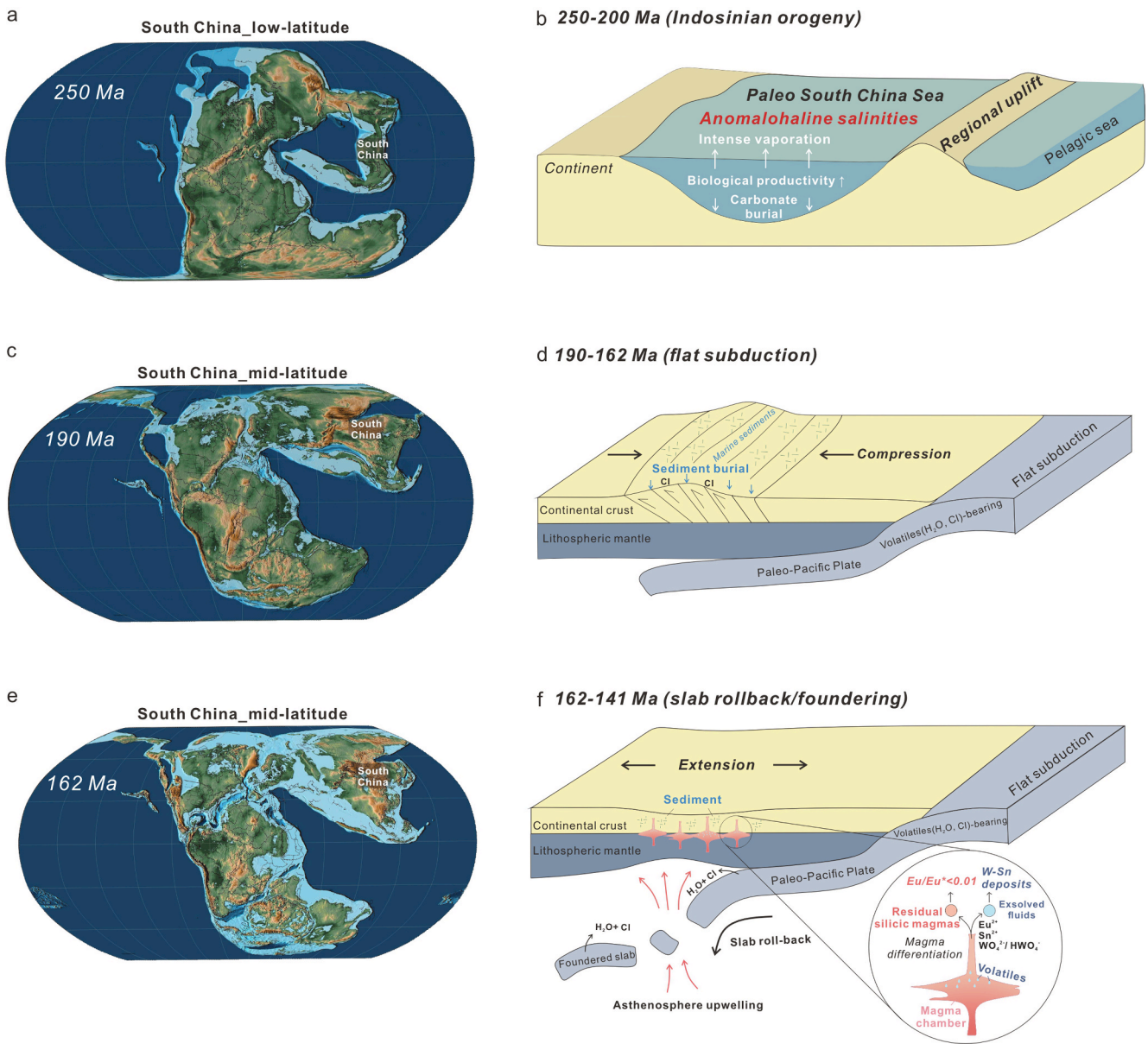


Fig. 9. Paleogeographic reconstruction in GPlates software for 250 Ma (a), 190 Ma (c) and 162 Ma (e) showing South China Block location. South China was positioned near the equator during the Permian-Triassic period (Indosinian), and subsequently drifted northward during the Jurassic-Cretaceous (Yanshanian). Data are from Scotese (2021). Tectonic evolution model of the South China Block during the Indosinian period (b) and the Yanshanian period (d, f).

Our calculation also shows that extensive fluid extraction under mildly reducing conditions may have also been important for W-Sn enrichment, which may explain the coincidence between low-Eu/Eu* granite formation and W-Sn mineralization in South China. Together with paleogeographic reconstruction results, we suggest that a critical source component of the Yanshannian granites may have come from the sedimentary strata deposited in a near-equator intracontinental sea in South China in the Permian-Triassic, which provided halogens and reduced C.

Data availability

Data are available through Mendeley data at https://doi.org/10.17632/k3cckwbwn3.1.

CRediT authorship contribution statement

Zi Ye: Writing – original draft, Visualization, Methodology, Investigation, Formal analysis, Data curation, Conceptualization. **Ming Tang:** Writing – review & editing, Supervision, Methodology, Funding acquisition, Conceptualization. **Xu Chu:** Writing – review & editing, Validation, Methodology.

Declaration of competing interest

The authors declare that they have no known competing financial interests or personal relationships that could have appeared to influence the work reported in this paper.

Acknowledgements

This work was financially supported by National Natural Science Foundation of China (grants 42125302, 42073026, and 41888101). We sincerely thank Xiaolei Wang for his guidance on oxygen isotope analysis. We also thank Hao Chen, Xuanyu Liu, Ziyi Guo, and Jiazhen Wang for their assistance with sample collection, and Junteng Lyu and Ziqi

Yang for helpful discussions. We are grateful to Executive Editor Hailiang Dong and Associate Editor Xiaoming Liu for handling the manuscript, as well as to the three anonymous reviewers for their insightful comments, which greatly improved the presentation of this work.

Appendix A. Supplementary material

Supplementary Material 1 includes sampling information and newly acquired geochemical data from this study, including major and trace element compositions of granites from South China and South Tibet, and zircon trace element and oxygen isotope data. Supplementary Material 2 includes major and trace element compositions of granites from South China and South Tibet compiled from previous studies. Supplementary Material 3 includes petrographic photographs of representative granites, cathodoluminescence images showing zircon oxygen isotope analysis spots, plots of zircon $\delta^{18}O$ values versus Th concentration and U concentrations, rhyolite-MELTS simulation results of feldspar crystallization proportions, and modeling of K-feldspar fractional crystallization effects on Ba/Th ratios. Supplementary Material 4 provides the calculation formulae and processes for Eu/Eu* variations during feldspar fractionation and fluid extraction, as well as calculations of W and Sn concentrations during fluid extraction.

Supplementary material to this article can be found online at https://doi.org/10.1016/j.gca.2025.07.028.

References

Bai, T.B., Koster van Groos, A.F., 1999. The distribution of Na, K, Rb, Sr, Al, Ge, Cu, W, Mo, La, and Ce between granitic melts and coexisting aqueous fluids. Geochim. Cosmochim. Acta 63, 1117–1131.

Bai, X.J., Liu, M., Hu, R.G., Fang, Y., Liu, X., Tang, B., Qiu, H.N., 2022. Well-constrained mineralization ages by integrated $^{40}Ar/^{39}Ar$ and U-Pb dating techniques for the Xitian W-Sn polymetallic deposit, South China. Econ. Geol. 117, 833–852.

Ballouard, C., Poujol, M., Boulvais, P., Branquet, Y., Tartèse, R., Vigneresse, J.L., 2016. Nb-Ta fractionation in peraluminous granites: a marker of the magmatic-hydrothermal transition. Geology 44, 231–234.

Bau, M., 1996. Controls on the fractionation of isovalent trace elements in magmatic and aqueous systems: evidence from Y/Ho, Zr/Hf, and lanthanide tetrad effect. Contrib. Miner. Petrol. 123, 323–333.

Borchert, M., Wilke, M., Schmidt, C., Rickers, K., 2010. Rb and Sr partitioning between haplogranitic melts and aqueous solutions. Geochim. Cosmochim. Acta 74, 1057–1076.

Brown, T., Pitfield, P., 2014. Tungsten, in: Critical Metals Handbook, pp. 385–413.

Burnham, A.D., Berry, A.J., Halse, H.R., Schofield, P.F., Cibin, G., Mosselmans, J.F.W., 2015. The oxidation state of europium in silicate melts as a function of oxygen fugacity, composition and temperature. Chem. Geol. 411, 248–259.

Cao, H.W., Pei, Q.M., Santosh, M., Li, G.M., Zhang, L.K., Zhang, X.F., Zhang, Y.H., Zou, H., Dai, Z.W., Lin, B., Tang, L., Yu, X., 2022. Himalayan leucogranites: a review of geochemical and isotopic characteristics, timing of formation, genesis, and rare metal mineralization. Earth Sci. Rev. 234, 104229.

Chen, B., Gu, H.O., Chen, Y., Sun, K., Chen, W., 2018. Lithium isotope behaviour during partial melting of metapelites from the Jiangnan Orogen, South China: Implications for the origin of REE tetrad effect of F-rich granite and associated rare-metal mineralization. Chem. Geol. 483, 372–384.

Chen, J.Y., Yang, J.H., Zhang, J.H., Zhu, Y.S., Yang, Z.G., 2023. Zircon reveals crystal-melt segregation processes in the genesis of cretaceous A-type granites and related cumulated rocks in southeastern China. Chem. Geol. 619.

Chen, S.C., Yu, J.J., Bi, M.F., 2021. Extraction of fractionated interstitial melt from a crystal mush system generating the late Jurassic high-silica granites from the Qitianling composite pluton, South China: implications for greisen-type tin mineralization. Lithos 382–383, 105952.

Chu, X., Ague, J.J., 2013. Phase equilibria for graphitic metapelite including solution of CO_2 in melt and cordierite: implications for dehydration, partial melting and graphite precipitation. J. Metam. Geol. 31, 843–862.

Dai, L., Wang, L., Lou, D., Li, Z.H., Dong, H., Ma, F., Li, F., Li, S., Yu, S., 2020. Slab rollback versus delamination: contrasting fates of flat-slab subduction and implications for South China evolution in the Mesozoic. J. Geophys. Res. Solid Earth 125, e2019JB019164.

Deng, Y., Li, J., Peng, T., Ma, Q., Song, X., Sun, X., Shen, Y., Fan, W., 2019. Lithospheric structure in the Cathaysia block (South China) and its implication for the late Mesozoic magmatism. Phys. Earth Planet. In. 291, 24–34.

Dong, Y., Zhang, G., Neubauer, F., Liu, X., Genser, J., Hauzenberger, C., 2011. Tectonic evolution of the Qinling orogen, China: review and synthesis. J. Asian Earth Sci. 41, 213–237.

Drake, M.J., Weill, D.F., 1975. Partition of Sr, Ba, Ca, Y, Eu^{2+}, Eu^{3+}, and other REE between plagioclase feldspar and magmatic liquid: an experimental study. Geochim. Cosmochim. Acta 39, 689–712.

Ewart, A., Griffin, W.L., 1994. Application of proton-microprobe data to trace-element partitioning in volcanic rocks. Chem. Geol. 117, 251–284.

Faure, M., Lin, W., Chu, Y., Lepvrier, C., 2016. Triassic tectonics of the Ailaoshan Belt (SW China): Early Triassic collision between the South China and Indochina Blocks, and Middle Triassic intracontinental shearing. Tectonophysics 683, 27–42.

Fedele, L., Lustrino, M., Melluso, L., Morra, V., Zanetti, A., Vannucci, R., 2015. Trace-element partitioning between plagioclase, alkali feldspar, Ti-magnetite, biotite, apatite, and evolved potassic liquids from Campi Flegrei (Southern Italy). Am. Mineral. 100, 233–249.

Gao, P., Zheng, Y.F., Zhao, Z.F., 2017. Triassic granites in South China: a geochemical perspective on their characteristics, petrogenesis, and tectonic significance. Earth Sci. Rev. 173, 266–294.

Gao, S., Wedepohl, K.H., 1995. The negative Eu anomaly in Archean sedimentary rocks: implications for decomposition, age and importance of their granitic sources. Earth Planet. Sci. Lett. 133, 81–94.

Gelman, S.E., Deering, C.D., Bachmann, O., Huber, C., Gutiérrez, F.J., 2014. Identifying the crystal graveyards remaining after large silicic eruptions. Earth Planet. Sci. Lett. 403, 299–306.

Gualda, G.A.R., Ghiorso, M.S., Lemons, R.V., Carley, T.L., 2012. Rhyolite-MELTS: a modified calibration of MELTS optimized for silica-rich, fluid-bearing magmatic systems. J. Petrol. 53, 875–890.

Guo, N.X., Zhao, Z., Gao, J.F., Chen, W., Wang, D.H., Chen, Y.C., 2018. Magmatic evolution and W-Sn-U-Nb-Ta mineralization of the Mesozoic Jiulongnao granitic complex, Nanling Range, South China. Ore Geol. Rev. 94, 414–434.

Henderson, P.B., 1984. Rare earth Element Geochemistry. Elsevier, Amsterdam.

Henson, S.A., Sanders, R., Madsen, E., 2012. Global patterns in efficiency of particulate organic carbon export and transfer to the deep ocean. Global Biogeochem. Cycles 26.

Hoskin, P.W.O., Schaltegger, U., 2003. The composition of zircon and igneous and metamorphic petrogenesis. Rev. Mineral. Geochem. 53, 27–62.

Hu, F., Jiang, H., Wan, B., Ducea, M.N., Gao, L., Wu, F.Y., 2024a. Latitude-dependent oxygen fugacity in arc magmas. Nat. Commun. 15, 6050.

Hu, R.Z., Gao, W., Fu, S.L., Su, W.C., Peng, J.T., Bi, X.W., 2024b. Mesozoic intracontinental metallogenesis in South China. Earth Sci. Front. 31, 226–238 in Chinese with English abstract.

Hu, R.Z., Zhou, M.F., 2012. Multiple Mesozoic mineralization events in South China—an introduction to the thematic issue. Mineral. Depos. 47, 579–588.

Hu, X., Jiang, D., Deng, G., Huang, F., 2024c. Rubidium isotope compositions of biotite in granites record magmatic-hydrothermal process and rare metal enrichments. Geochim. Cosmochim. Acta 382, 26–39.

Huang, C., Wang, H., Yang, J.H., Ramezani, J., Yang, C., Zhang, S.B., Yang, Y.H., Xia, X. P., Feng, L.J., Lin, J., Wang, T.T., Ma, Q., He, H.Y., Xie, L.W., Wu, S.T., 2019. SA01—A proposed zircon reference material for microbeam U-Pb age and Hf-O isotopic determination. Geostand. Geoanal. Res. 44, 103–123.

Huang, H.Q., Li, X.H., Li, Z.X., Li, W.X., 2015. Formation of the Jurassic South China large granitic province: insights from the genesis of the Jiufeng pluton. Chem. Geol. 401, 43–58.

Irber, W., 1999. The lanthanide tetrad effect and its correlation with K/Rb, Eu/Eu*, Sr/Eu, Y/Ho, and Zr/Hf of evolving peraluminous granite suites. Geochim. Cosmochim. Acta 63, 489–508.

Ji, W., Faure, M., Lin, W., Chen, Y., Chu, Y., Xue, Z., 2018. Multiple emplacement and exhumation history of the late Mesozoic Dayunshan–Mufushan batholith in Southeast China and its tectonic significance: 1. Structural analysis and geochronological constraints. J. Geophys. Res. Solid Earth 123, 689–710.

Jiang, C.H., Du, D.H., Wang, X.L., 2022a. Crust-penetrating magmatic systems, degassing processes, and environmental effects in intracontinental settings. Acta Petrol. Sin. 38, 1360–1374 in Chinese with English abstract.

Jiang, J., Mao, Y., Hu, X., 2022b. Factors on the Mesozoic transition from flat to steep subduction of the Paleo-Pacific Plate beneath South China: thickened oceanic crust and subduction rate. Geochem. Geophys. Geosyst. 23, e2022GC010523.

Kasten, S., Jørgensen, B.B., 2000. Sulfate reduction in marine sediments. In: Schulz, H.D., Zabel, M. (Eds.), Marine Geochemistry. Springer, Berlin, Heidelberg, pp. 263–281.

Kemp, A.I., Hawkesworth, C.J., Foster, G.L., Paterson, B.A., Woodhead, J.D., Hergt, J.M., Gray, C.M., Whitehouse, M.J., 2007. Magmatic and crustal differentiation history of granitic rocks from Hf-O isotopes in zircon. Science 315, 980–983.

Lehmann, B., 1990. Metallogeny of Tin. Springer, Berlin, Heidelberg.

Lehmann, B., 2021. Formation of tin ore deposits: a reassessment. Lithos 402–403.

Li, H., Wu, J.H., Evans, N.J., Jiang, W.C., Zhou, Z.K., 2018. Zircon geochronology and geochemistry of the Xianghualing A-type granitic rocks: Insights into multi-stage Sn-polymetallic mineralization in South China. Lithos 312–313, 1–20.

Li, S., Suo, Y., Li, X., Zhou, J., Santosh, M., Wang, P., Wang, G., Guo, L., Yu, S., Lan, H., Dai, L., Zhou, Z., Cao, X., Zhu, J., Liu, B., Jiang, S., Wang, G., Zhang, G., 2019. Mesozoic tectono-magmatic response in the East Asian ocean-continent connection zone to subduction of the Paleo-Pacific Plate. Earth Sci. Rev. 192, 91–137.

Li, X.H., Li, W.X., Wang, X.C., Li, Q.L., Liu, Y., Tang, G.Q., 2009a. The role of mantle-derived magmas in the early Yanshanian granite formation in the Nanling region: constraints from in-situ zircon Hf-O isotopes. Sci. China Ser. D Earth Sci. 39, 872–887 in Chinese with English abstract.

Li, X.H., Li, W.X., Li, Z.X., Lo, C.H., Wang, J., Ye, M.F., Yang, Y.H., 2009b. Amalgamation between the Yangtze and Cathaysia Blocks in South China: Constraints from SHRIMP U-Pb zircon ages, geochemistry and Nd-Hf isotopes of the Shuangxiwu volcanic rocks. Precambr. Res. 174, 117–128.

Li, Z.X., Li, X.H., 2007. Formation of the 1300-km-wide intracontinental orogen and postorogenic magmatic province in Mesozoic South China: a flat-slab subduction model. Geology 35, 179–182.

Lin, S., Xing, G., Davis, D.W., Yin, C., Wu, M., Li, L., Jiang, Y., Chen, Z., 2018. Appalachian-style multi-terrane Wilson cycle model for the assembly of South China. Geology 46, 319–322.
Lin, W., Faure, M., Wang, Q., Monié, P., Panis, D., 2005. Triassic polyphase deformation in the Feidong-Zhangbaling Massif (eastern China) and its place in the collision between the North China and South China blocks. J. Asian Earth Sci. 25, 121–136.
Liu, J.X., Wang, S., Wang, X.L., Du, D.H., Xing, G.F., Fu, J.M., Chen, X., Sun, Z.M., 2020a. Refining the spatio-temporal distributions of Mesozoic granitoids and volcanic rocks in SE China. J. Asian Earth Sci. 201.
Liu, P., Mao, J., Jian, W., Mathur, R., 2020b. Fluid mixing leads to main-stage cassiterite precipitation at the Xiling Sn polymetallic deposit, SE China: evidence from fluid inclusions and multiple stable isotopes (H-O-S). Mineral. Depos. 55, 1233–1246.
Liu, T., Hu, Z., Zhang, D., Li, S., Cheng, C., Zhou, L., Wang, G., Wang, X., Wang, Z., 2023. The timing of the initial collision between the South and North China blocks constraining from the sediments in the eastern Sichuan Basin. Sci. Rep. 13, 22378.
Loucks, R.R., Fiorentini, M.L., Henríquez, G.J., 2020. New magmatic oxybarometer using trace elements in zircon. J. Petrol. 61.
Lu, H.Z., Liu, Y., Wang, C., Xu, Y., Li, H., 2003. Mineralization and fluid inclusion study of the Shizhuyuan W-Sn-Bi-Mo-F skarn deposit, Hunan Province, China. Econ. Geol. 98, 955–974.
Luo, X.L., Wu, C.Z., She, J.X., Brzozowski, M.J., Du, D.H., An, S., Li, W., 2024. Understanding the extreme differentiation of granitic magmas through elemental geochemistry and Fe isotope signatures. Geochim. Cosmochim. Acta 380, 31–47.
Luo, Z.H., Lu, X.X., Guo, S.F., Sun, J., Chen, B.H., Huang, F., Yang, Z.F., 2008. Magmatic fluid metallogenic system. Acta Petrol. Sin. 24, 2669–2678 in Chinese with English abstract.
Ma, X., Wang, H., Lehmann, B., Guo, C., Mao, J., 2024. Control of magmatic halogen composition and redox state on the zonation of metal mineralization across active continental margins: perspectives from the world-class South China metallogenic province. Chem. Geol. 669.
Mao, J.W., Cheng, Y.B., Chen, M.H., Franco, P., 2013. Major types and time-space distribution of Mesozoic ore deposits in South China and their geodynamic settings. Mineral. Depos. 48, 267–294.
Meng, Q.R., Zhang, G.W., 2000. Geologic framework and tectonic evolution of the Qinling orogen, central China. Tectonophysics 323, 183–196.
Monecke, T., Kempe, U., Trinkler, M., Thomas, R., Dulski, P., Wagner, T., 2011. Unusual rare earth element fractionation in a tin-bearing magmatic-hydrothermal system. Geology 39, 295–298.
Paton, C., Hellstrom, J., Paul, B., Woodhead, J., Hergt, J., 2011. Iolite: Freeware for the visualisation and processing of mass spectrometric data. J. Anal. At. Spectrom. 26.
Ptáček, M.P., Dauphas, N., Greber, N.D., 2020. Chemical evolution of the continental crust from a data-driven inversion of terrigenous sediment compositions. Earth Planet. Sci. Lett. 539, 116090.
Rollinson, H., Pease, V., 2021. Using Geochemical Data: To Understand Geological Processes, second ed. Cambridge University Press, Cambridge.
Romer, R.L., Kroner, U., 2016. Phanerozoic tin and tungsten mineralization—tectonic controls on the distribution of enriched protoliths and heat sources for crustal melting. Gondw. Res. 31, 60–95.
Rudnick, R.L., Gao, S., 2014. Composition of the continental crust. Treatise Geochem. 4, 1–51.
Scotese, C.R., 2021. An atlas of Phanerozoic paleogeographic maps: the seas come in and the seas go out. Annu. Rev. Earth Planet. Sci. 49, 679–728.
Shinohara, H., Kazahaya, K., Lowenstern, J.B., 1995. Volatile transport in a convecting magma column: implications for porphyry Mo mineralization. Geology 23, 1091–1094.
Shu, L., Faure, M., Wang, B., Zhou, X., Song, B., 2008. Late Palaeozoic-Early Mesozoic geological features of South China: response to the Indosinian collision events in Southeast Asia. C. R. Geosci. 340, 151–165.
Shu, L., Wang, B., Cawood, P.A., Santosh, M., Xu, Z., 2015. Early Paleozoic and early Mesozoic intraplate tectonic and magmatic events in the Cathaysia Block, South China. Tectonics 34, 1600–1621.
Song, M., Shu, L., Santosh, M., 2016. Early Mesozoic granites in the Nanling Belt, South China: implications for intracontinental tectonics associated with stress regime transformation. Tectonophysics 676, 148–169.
Stix, J., Gorton, M.P., 1990. Variations in trace element partition coefficients in sanidine in the Cerro Toledo Rhyolite, Jemez Mountains, New Mexico: effects of composition, temperature, and volatiles. Geochim. Cosmochim. Acta 54, 2697–2708.
Sundell, K.E., Macdonald, F.A., Puetz, S.J., 2024. Does zircon geochemistry record global sediment subduction? Geology 52, 282–286.
Tang, M., Ji, W.Q., Chu, X., Wu, A., Chen, C., 2020. Reconstructing crustal thickness evolution from europium anomalies in detrital zircons. Geology 49, 76–80.
Valley, J.W., Lackey, J.S., Cavosie, A.J., Clechenko, C.C., Spicuzza, M.J., Basei, M.A.S., Bindeman, I.N., Ferreira, V.P., Sial, A.N., King, E.M., Peck, W.H., Sinha, A.K., Wei, C. S., 2005. 4.4 billion years of crustal maturation: oxygen isotope ratios of magmatic zircon. Contrib. Miner. Petrol. 150, 561–580.
Wang, T., Tong, Y., Huang, H., Zhang, H., Guo, L., Li, Z., Wang, X., Eglington, B., Li, S., Zhang, J., Donskaya, T.V., Petrov, O., Zhang, L., Song, P., Zhang, X., Wang, C., 2023. Granitic record of the assembly of the asian continent. Earth Sci. Rev. 237, 104298.
Wang, X.L., Coble, M.A., Valley, J.W., Shu, X.J., Kitajima, K., Spicuzza, M.J., Sun, T., 2014. Influence of radiation damage on late Jurassic zircon from southern China: evidence from in situ measurements of oxygen isotopes, laser Raman, U-Pb ages, and trace elements. Chem. Geol. 389, 122–136.
Wang, Y., Fan, W., Cawood, P.A., Li, S., 2008. Sr–Nd–Pb isotopic constraints on multiple mantle domains for Mesozoic mafic rocks beneath the South China Block hinterland. Lithos 106, 297–308.
Wang, Y., Fan, W., Zhang, G., Zhang, Y., 2013. Phanerozoic tectonics of the South China Block: Key observations and controversies. Gondw. Res. 23, 1273–1305.
Weill, D.F., Drake, M.J., 1973. Europium anomaly in plagioclase feldspar: experimental results and semiquantitative model. Science 180, 1059–1060.
White, J.C., 2003. Trace-element partitioning between alkali feldspar and peralkalic quartz trachyte to rhyolite magma. Part II: empirical equations for calculating trace-element partition coefficients of large-ion lithophile, high field-strength, and rare-earth elements. Am. Mineral. 88, 330–337.
Wu, F.Y., Guo, C.L., Hu, F.Y., Liu, X.C., Zhao, J.X., Li, X.F., Qin, K.Z., 2023. Petrogenesis and metallogenesis of highly fractionated granites in the Nanling region. Acta Petrol. Sin. 39, 1–36 in Chinese with English abstract.
Xu, C., Deng, Y., Barnes, C.G., Shi, H., Pascal, C., Li, Y., Gao, S., Jiang, D., Xie, J., Ma, C., 2023. Offshore-onshore tectonomagmatic correlations: towards a late Mesozoic non-Andean-type Cathaysian continental margin. Earth Sci. Rev. 240, 104382.
Xu, X.B., Zhang, Y.Q., Jia, D., Shu, L.S., Wang, R.R., 2009. Early to Middle Mesozoic tectonic evolution of South China. Geol. China 36, 573–593 in Chinese with English abstract.
Xu, X., 2023. Late Triassic to Middle Jurassic tectonic evolution of the South China Block: geodynamic transition from the Paleo-Tethys to the Paleo-Pacific regimes. Earth-Sci. Rev. 241.
Yu, J., Cai, Y., Sun, T., Jiang, W., Zhang, R., Griffin, W.L., Mao, Z., Xia, L., 2023. Distribution and enrichment of rare metal elements in the basement rocks of South China: Controls on rare-metal mineralization. Ore Geol. Rev. 163.
Yuan, S., Williams-Jones, A.E., Romer, R.L., Zhao, P., Mao, J., 2019. Protolith-related thermal controls on the decoupling of Sn and W in Sn-W metallogenic provinces: insights from the Nanling Region, China. Econ. Geol. 114, 1005–1012.
Zajacz, Z., Halter, W.E., Pettke, T., Guillong, M., 2008. Determination of fluid/melt partition coefficients by LA-ICPMS analysis of co-existing fluid and silicate melt inclusions: controls on element partitioning. Geochim. Cosmochim. Acta 72, 2169–2197.
Zhang, H., Lu, Q.T., Wang, X.L., Han, S., Liu, L., Gao, L., Wang, R., Hou, Z.Q., 2023a. Seismically imaged lithospheric delamination and its controls on the Mesozoic magmatic province in South China. Nat. Commun. 14, 2718.
Zhang, L., Jiang, S.Y., Romer, R.L., Su, H.M., 2023b. Relative importance of magmatic and hydrothermal processes for economic Nb-Ta-W-Sn mineralization in a peraluminous granite system: the Zhaojinggou rare-metal deposit, Northern China. GSA Bull.
Zhang, Y., Yang, J.H., Chen, J.Y., Wang, H., Xiang, Y.X., 2017. Petrogenesis of Jurassic tungsten-bearing granites in the Nanling Range, South China: evidence from whole-rock geochemistry and zircon U-Pb and Hf-O isotopes. Lithos 278–281, 166–180.
Zhang, Z.Y., Hou, Z.Q., Lü, Q.T., Zhang, X.W., Pan, X.F., Fan, X.K., Zhang, Y.Q., Wang, C. G., Lü, Y.J., 2023c. Crustal architectural controls on critical metal ore systems in South China based on Hf isotopic mapping. Geology 51, 738–742.
Zhao, L., Tang, H., Mitchell, R.N., Li, Q.L., Zhou, X.W., Zhai, M.G., 2023. The joining of North and South China during the Permian: coherent metamorphic evidence from East Asia orogenesis. Tectonics 42 e2023TC007916.
Zhao, P., Chu, X., Williams-Jones, A.E., Mao, J., Yuan, S., 2021. The role of phyllosilicate partial melting in segregating tungsten and tin deposits in W-Sn metallogenic provinces. Geology 50, 121–125.
Zhao, P., Yuan, S., Williams-Jones, A.E., Romer, R.L., Yan, C., Song, S., Mao, J., 2022a. Temporal separation of W and Sn mineralization by temperature-controlled incongruent melting of a single protolith: evidence from the Wangxianling area, Nanling region, South China. Econ. Geol. 117, 667–682.
Zhao, P., Zajacz, Z., Tsay, A., Yuan, S., 2022b. Magmatic-hydrothermal tin deposits form in response to efficient tin extraction upon magma degassing. Geochim. Cosmochim. Acta 316, 331–346.
Zhou, X., Sun, T., Shen, W., Shu, L., Niu, Y., 2006. Petrogenesis of Mesozoic granitoids and volcanic rocks in South China: a response to tectonic evolution. Episodes 29, 26–33.
Zhou, X.M., Li, W.X., 2000. Origin of late Mesozoic igneous rocks in Southeastern China: implications for lithosphere subduction and underplating of mafic magmas. Tectonophysics 326, 269–287.
Zou, X., Qin, K., Han, X., Li, G., Evans, N.J., Li, Z., Yang, W., 2019. Insight into zircon REE oxy-barometers: a lattice strain model perspective. Earth Planet. Sci. Lett. 506, 87–96.